A 3D Wideband Geometry-Based Stochastic Model for UAV Air-to-Ground Channels

Hengtai Chang[1], Ji Bian[1], Cheng-Xiang Wang[2,3], Zhiquan Bai[1], Jian Sun[1], and Xiqi Gao[2]

[1]Shandong Provincial Key Lab of Wireless Communication Technologies, Shandong Unviersity, Jinan, Shandong, 250100, China.
[2]School of Information Science and Engineering, Southeast University, Nanjing, 210096, China.
[3]Institute of Sensors, Signals and Systems, School of Engineering and Physical Sciences, Heriot-Watt University,
Edinburgh, EHl4 4AS, UK.
Email: hunter_chang@126.com, bianjimail@163.com, cheng–xiang.wang@hw.ac.uk., zqbai@sdu.edu.cn,
sunjian@sdu.edu.cn, xqgao@seu.edu.cn.

Abstract—Air-to-ground (A2G) communication plays an important role in ensuring reliable communication links between unmanned aerial vehicles (UAVs) and ground terminals. This paper presents a wideband truncated ellipsoidal shaped scattering region (TESR) geometry based stochastic model (GBSM) for Multiple-Input-Multiple-Output (MIMO) A2G channels. The proposed model contains a line-of-sight (LoS) component, a ground reflection component, and truncated ellipsoid scattering components. Based on the proposed GBSM, some important statistical properties like space-time-correlation-function (STCF) and Doppler power spectrum density (PSD) are derived. The impacts of elevation angle and UAV altitude on A2G channel characteristics are analyzed. Finally, excellent agreement is achieved between measurement data and simulation results of temporal auto correlation functions (ACFs), demonstrating applicability of the proposed model.

Index Terms—Unmanned aerial vehicles, MIMO air-to-ground channel models, channel characteristics, GBSM.

I. INTRODUCTION

In recent years, UAVs have attracted significant attention from various fields due to their high mobility and low cost [1]–[3]. For example, in disaster rescue and remote space sensing, UAVs can perform the task better and quicker than traditional methods. Besides, benefiting from the progress of battery power and information technologies, the advanced UAVs can serve as the wireless communication relays and airborne base stations due to their maneuverability and flexibility for on-demand deployment. Since channel models play a fundamental role in the communication system design and performance evaluation [4], A2G channel models with good accuracy-complexity-generality tradeoff are urgently needed.

Compared with traditional wireless communication channels, A2G channels show numerous unique properties. In A2G communications, transmitters (TX) and receivers (RX) can move in three-dimensional (3D) environments which means that the A2G channel models must be 3D. Besides, TX and RX can stay at different altitudes. Therefore, the elevation angles and altitudes of the UAVs should be taken into account while constructing A2G channel models. Meanwhile, the characteristics of the A2G channel depend on the communication environments to a great extent. For the A2G channels in open field scenarios such as suburban and over-water, the LoS

component contributes to the main received power. But for the A2G channel in complex environments like urban scenario, the multi-path propagation will have great impacts on the channel properties [11].

In the literature, many UAV communication channel models were proposed and channel measurements were carried out [5]–[15]. In [5]–[8], a series of measurement campaigns were conducted to investigate the channel characteristics such as path loss exponent (PLE) and shadowing of A2G channels. Based on channel measurement results, empirical A2G channel models were built to characterize the channel properties depending on experimental setups, such as the UAV flight altitude, the distance between UAV and ground terminal, and the scenario. Empirical channel models can reflect the real channels, but the measurement equipment is expensive and the measurement campaigns are time consuming. In [9], a statistical model for A2G channels in an urban environment based on a ray-tracing method was proposed. In [10], the channels between UAVs and vessels were studied based on the Finite-Difference-Time-Domain (FDTD) method. As typical deterministic channel modeling methods, ray-tracing and FDTD methods are quite accurate for given communication scenarios but not sufficiently flexible to describe the general UAV communication environments. Therefore, the feasibility of deterministic channel models is limited.

On the contrary, GBSM method is a stochastic channel modeling method that has been widely used to mimic wireless channels due to its good balance between accuracy, complexity, and easy to use. In [12]–[14], GBSMs for UAV scenarios based on single cylinder geometry model were proposed to describe the A2G channel environments and some channel characteristics such as space correlation function and temporal correlation functions were analyzed. However, existing UAV GBSMs are mostly based on the narrow band assumption, wherein different rays have the same time delay that could not describe the real A2G channel. In [15] and [16], angles of arrival (AoAs) for A2G channels were analyzed based on a wide band slant ellipsoid geometric channel model. However, the mobility of both UAVs and ground terminals is neglected and the investigated parameters are limited to AoAs and

channel capacities, which are not exhaustive enough to present UAV channel characteristics.

In this paper, we propose a novel 3D truncated ellipsoid wideband A2G GBSM to describe the A2G channel. Different from vehicle-to-vehicle or mobile-to-mobile ellipsoid channel models [21], the proposed channel model is a slant ellipsoid model taking into account the elevation angle of A2G communications. In addition, for A2G communication scenarios, scatterers like buildings and hills cannot be distributed in the air or underground. Thus, in order to improve the accuracy, in our model, scatterers are only distributed on the cross section of slant ellipsoid and ground plane. Based on the proposed model, we derive and analyze some important channel characteristics including STCF and Doppler PSD. At last, some useful conclusions and future research directions are given.

The rest of this paper is organized as follows. In Section II, the 3D wideband truncated ellipsoid GBSM is described. In Section III, some significant channel characteristics are analyzed based on the proposed model. Section IV gives the simulation results and analysis. Section V concludes the whole paper and points out the future works.

II. 3D WIDEBAND MIMO TRUNCATED ELLIPSOID GBSM

The general UAV-MIMO A2G communication system is shown in Fig. 1. TX with n_T transmit antennas is equipped on the UAV suspending in the air and can move in the 3D space, while RX with n_R receive antennas is located on the ground with a certain height. In order to facilitate calculation, a 2×2 UAV-MIMO channel, i.e., $n_T = n_R = 2$ is assumed and it is not difficult to further construct a uniform linear array with an arbitrary number of antenna elements. Since UAVs usually carry out complex maneuvers such as climbing, diving, and circling, the velocity direction of TX should be described using both azimuth and elevation angles. Here γ_T and ξ_T are azimuth and elevation angels of the TX moving direction, respectively. As for the RX, since the ground terminals only move on the ground plane, the velocity direction can be simply described by azimuth angle γ_R.

The proposed GBSM contains a LoS component, a reflection component, and scattering components. In Fig. 1, R denotes the reflecting point on the ground, and the multiple confocal ellipsoids taking transceivers as focal points represent the time delay line (TDL) structure and have N_l effective scatterers on the lth ellipsoid, where $l = 1, 2, ..., L$ and L is the total ellipsoids number. Considering that scatterers cannot be distributed in high altitude or underground, we suppose that they are only distributed on and near the ground. In detail, the scattering region on the ground is the cross sections of ellipsoids and the ground plane. Since that cross section of a ellipsoid is a ellipse, we can use an expression of ellipse to represent the scattering region on the ground. Then, since that scatterers such as buildings usually have vertical straight structure with certain heights, an elliptical cylinder could be constructed to represent scattering region in 3D space based on the elliptical cross section, which can be represented by shade elliptical cylinder in Fig. 1. Note that the height of scatters are
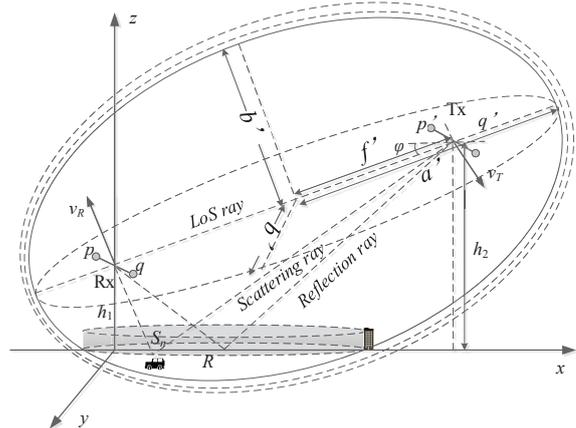

Fig. 1. A 3D GBSM for A2G channels.

much lower than the scale of ellipsoids, the scatter distributed on the elliptical cylinder still can be regarded as having the same time delay.

In order to obtain the formula expression of elliptical cross section, we refer to coordinate transform method proposed in [16]. $x' - y' - z'$ is a new coordinate taking the center of slant ellipsoid as origin and taking the major axis of slant ellipsoid as x-axis. The cross section of slant ellipsoid and ground plane $z = 0$ can be expressed in $x' - y' - z'$ as

$$\frac{x'^2}{(a')^2} + \frac{y'^2}{(b')^2} + \frac{(mx' - h'_s)^2}{(b')^2} = 1 \tag{1}$$

where $m = \cot(\varphi)$, a', b', and f' denote the major axis, minor axis, and focal length of the slant ellipsoid, respectively, and $h'_s = f' + h_1/\sin(\varphi)$. Thus, the major and minor axis of intersected ellipse can be calculated as

$$a = \frac{x'_{\max} - x'_{\min}}{2 \sin \varphi} \tag{2}$$

$$b = \left| \sqrt{a'^2 - \frac{a'^2}{b'^2}[mx'_{\text{off}} - h_s']^2 - x'^2_{\text{off}}} \right| \tag{3}$$

where $x'_{\max}$ and $x'_{\min}$ denote the x-value of the intersected ellipse major axis endpoints, and x'_{off} is the center of intersected ellipse. They can be expressed as

$$x'_{\max} = \frac{a^2 m h'_s + \sqrt{a^2 b^2 (b^2 + a^2 m^2 - h_s'^2)}}{b^2 + a^2 m^2} \tag{4}$$

$$x'_{\min} = \frac{a^2 m h'_s - \sqrt{a^2 b^2 (b^2 + a^2 m^2 - h_s'^2)}}{b^2 + a^2 m^2} \tag{5}$$

$$x'_{\text{off}} = \frac{x'_{\max} + x'_{\min}}{2}. \tag{6}$$

Converting back to the origin coordinate $x - y - z$ and applying the ellipse formula, we can get the expression of the elliptical

cross section as

$$\frac{(x-x_{\text{off}})^2}{(a)^2} + \frac{y^2}{(b)^2} = 1$$

where $x_{\text{off}} = x'_{\text{off}}/\sin(\varphi)$ denotes the center of elliptical cross section in coordinate $x-y-z$.

III. CHANNEL CHARACTERISTICS

According to the TDL concept, the complex impulse response of MIMO fading channel can be represented by $h_{pq}(t,\tau') = \sum_{l=1}^{L} c_l h_{l,pq}(t)\delta(\tau'-\tau_l')$, in which c_l denotes the gain of the lth tap, $h_{l,pq}(t)$ is the complex lth tap coefficient between the pth RX antenna and the qth TX antenna, and τ_l' is propagation delay of the lth tap.

From the above GBSM, the first tap is the LoS component, the second tap is the reflection component, and the ellipsoid scattering components represent the $3\text{rd}-L$th taps. The complex tap coefficients of different taps can be expressed by

$$
\begin{aligned}
h_{1,pq}(t) &= h_{pq}^{\text{LoS}}(t) = e^{-jk_0 d(p,q)}\\
&\times e^{j2\pi f_{Tm}t[\cos(\alpha_T^{\text{LoS}}-\gamma_T)\cos\beta_T^{\text{LoS}}\cos\xi_T+\sin\beta_T^{\text{LoS}}\sin\xi_T]}\\
&\times e^{j2\pi f_{Rm}t[\cos(\alpha_R^{\text{LoS}}-\gamma_R)\cos\beta_R^{\text{LoS}}]}
\end{aligned}
\tag{7}
$$

$$
\begin{aligned}
h_{2,pq}(t) &= h_{pq}^{\text{Ref}}(t) = e^{-j(\theta_r+k_0(d(p,R)+d(R,q)))}\\
&\times e^{j2\pi f_{Tm}t[\cos(\alpha_T^{\text{Ref}}-\gamma_T)\cos\beta_T^{\text{Ref}}\cos\xi_T+\sin\beta_T^{\text{Ref}}\sin\xi_T]}\\
&\times e^{j2\pi f_{Rm}t[\cos(\alpha_R^{\text{Ref}}-\gamma_R)\cos\beta_R^{\text{Ref}}]}
\end{aligned}
\tag{8}
$$

$$
\begin{aligned}
h_{l,pq}(t) &= h_{l,pq}^{\text{Sca}}(t) = \lim_{N\to\infty}\sum_{n=1}^{N_l}\frac{1}{\sqrt{N_l}}\\
&\times e^{j2\pi f_{Tm}t[\cos(\alpha_T^{\text{Sca}}-\gamma_T)\cos\beta_T^{\text{Sca}}\cos\xi_T+\sin\beta_T^{\text{Sca}}\sin\xi_T]}\\
&\times e^{j2\pi f_{Rm}t[\cos(\alpha_R^{\text{Sca}}-\gamma_R)\cos\beta_R^{\text{Sca}}]}\\
&\times e^{-j(\theta_n+k_0(d(p,s_n)+d(s_n,q)))}, (l>2).
\end{aligned}
\tag{9}
$$

For the scattering ray, α_R^{Sca}, β_R^{Sca}, α_T^{Sca}, and β_T^{Sca} denote azimuth AoA (AAoA), elevation AoA (EAoA), azimuth AoD (AAoD), and elevation AoD (EAoD), respectively. The relationship between AoA and AoD can be obtained by geometric algorithm. Since that $\min\{D,h_1\} >> \max\{\delta_T,\delta_R\}$. The scattering angular relationship can be expressed as

$$\alpha_T^{\text{Sca}} = \arcsin\left(\frac{z_n-h_2}{\sqrt{(x_n-Dm)^2+y_n^2}}\right) \tag{10}$$

$$\beta_T^{\text{Sca}} = \arctan\left(\frac{y_n}{\sqrt{(x_n-Dm)^2+y_n^2}}\right) \tag{11}$$

where x_n, y_n, and z_n are the x, y, and z components of s_n 3D location, which can be obtained by calculating the intersection of elliptical cylinder and incidence ray, i.e.,

$$
\begin{cases}
x_n = \frac{x_{\text{off}}b^2+ab\sqrt{a^2\tan\alpha_R^{\text{Sca}}+b^2-x_{\text{off}}^2\tan^2\alpha_T^{\text{Sca}}}}{b^2+a^2\tan^2\alpha_R^{\text{Sca}}}\\
y_n = x_n\tan\alpha_R^{\text{Sca}}\\
z_n = \sqrt{x_n^2+y_n^2}\tan\beta_R^{\text{Sca}}.
\end{cases}
\tag{12}
$$

In the case of LoS and reflection components, we can get $\alpha_T^{\text{LoS}} = -\pi$, $\alpha_R^{\text{LoS}} = 0$, $\beta_T^{\text{LoS}} = -\varphi$, and $\beta_R^{\text{LoS}} = \varphi$, $\alpha_T^{\text{Ref}} = -\pi$, $\alpha_R^{\text{Ref}} = 0$, $\beta_T^{\text{Ref}} = \beta_R^{\text{Ref}} = \arctan(\frac{h_1+h_2}{D\sin\varphi})$.

In addition, $k_0 = 2\pi/\lambda$ refers to the wave number, where λ is the wavelength. The random phase shift θ_r and θ_n caused by reflection and scattering are independent identically distributed (i.i.d) random variables and uniformly distributed in $(0,2\pi)$. Other significant parameters are listed and defined in Table I.

Because in the reference model, we assume that there are infinite scatterers in each tap (i.e., $N_l \to \infty$), EAoA and AAoA can be random variables following certain distributions. In this paper, we adopt the von-Mises distribution, which is a widely used distribution representing the scatterers distribution in wireless channels, to describe AAoA. At the same time, since the distribution of scatterers in vertical direction is limited, cosine distribution is used to describe the EAoA [14]. Next, based on the wideband GBSM, the STCF and Doppler PSD can be derived. Under the wide-sense stationary uncorrelation-scattering (WSSUS) condition, correlation properties of two sub-channels are determined by correlation properties of each tap, and we assume that there is no correlation between different taps. Thus, the STCF can be computed as

$$\rho_{h_{l,pq}h_{l,p'q'}}(t,\tau) = \mathbf{E}[h_{l,pq}(t)h_{l,p'q'}^*(t-\tau)] \tag{13}$$

where $\mathbf{E}[\cdot]$ denotes the expectation operation and $()^*$ is the complex conjugate operation. substituting (7)-(9) into (17), we can obtain STCF of each tap. In terms of the first tap, i.e., LoS component, we have

$$
\begin{aligned}
\rho_{h_{1,pq}h_{1,p'q'}}(t,\tau) &= e^{-jk_0(d(p,q)-d(p',q'))}\\
&\times e^{j2\pi f_{Tm}\tau[\cos(\alpha_T^{\text{LoS}}-\gamma_T)\cos\beta_T^{\text{LoS}}\cos\xi_T+\sin\beta_T^{\text{LoS}}\sin\xi_T]}\\
&\times e^{j2\pi f_{Rm}\tau[\cos(\alpha_R^{\text{LoS}}-\gamma_R)\cos\beta_R^{\text{LoS}}]}.
\end{aligned}
\tag{14}
$$

In case of the second tap, i.e., the reflection component, it is written as

$$
\begin{aligned}
\rho_{h_{2,pq}h_{2,p'q'}}(t,\tau) &= e^{-jk_0(d(p,R')+d(R',q)-d(p',R')-d(R',q'))}\\
&\times e^{j2\pi f_{Tm}\tau[\cos(\alpha_T^{\text{Ref}}-\gamma_T)\cos\beta_T^{\text{Ref}}\cos\xi_T+\sin\beta_T^{\text{Ref}}\sin\xi_T]}\\
&\times e^{j2\pi f_{Rm}\tau[\cos(\alpha_R^{\text{Ref}}-\gamma_R)\cos\beta_R^{\text{Ref}}]}.
\end{aligned}
\tag{15}
$$

For the other taps containing scattering components, we have

$$
\begin{aligned}
\rho_{h_{l,pq}h_{l,p'q'}}(t,\tau) &= \int_0^{2\pi}\int_{\beta_\mu-\beta_m}^{\beta_\mu+\beta_m} e^{-jk_0(d(p,S_n)+d(S_n,q))}\\
&\times e^{jk_0(d(p',S_n)+d(S_n,q'))}\\
&\times e^{j2\pi f_{Tm}\tau[\cos(\alpha_T^{\text{Sca}}-\gamma_T)\cos\beta_T^{\text{Sca}}\cos\xi_T+\sin\beta_T^{\text{Sca}}\sin\xi_T]}\\
&\times e^{j2\pi f_{Rm}\tau[\cos(\alpha_R^{\text{Sca}}-\gamma_R)\cos\beta_R^{\text{Sca}}]}\\
&\times f(\alpha_R^{\text{Sca}})f(\beta_R^{\text{Sca}})d\alpha_R^{\text{Sca}}d\beta_R^{\text{Sca}}, (l>2)
\end{aligned}
\tag{16}
$$

where $f(\alpha_R^{\text{Sca}})$ and $f(\beta_R^{\text{Sca}})$ are probability density functions (PDFs) of α_R^{Sca} and β_R^{Sca} with von-Mises distribution and cosine distribution. They can be expressed by

$$f(\alpha_R^{\text{Sca}}) = \frac{e^{k\cos(\alpha_R^{\text{Sca}}-\alpha_\mu)}}{2\pi I_0(k)}, 0\le\alpha_R^{\text{Sca}}\le 2\pi \tag{17}$$

$$f(\beta_R^{\text{Sca}}) = \frac{\pi}{4\beta_m}\cos(\frac{\pi}{2}\frac{\beta_R^{\text{Sca}} - \beta_\mu}{\beta_m}),$$
$$\beta_\mu - \beta_m \le \beta_R^{\text{Sca}} \le \beta_\mu + \beta_m \quad (18)$$

for von-Mises distribution that describe the AAoA, $I_0()$ is the zeroth-order modified Bessel function of the first kind, $\alpha_\mu \in [0, 2\pi]$ is the mean angle at which the scatterers are distributed in the horizontal direction, and parameter k controls the spread around the mean angle. For cosine distribution that describe the EAoA, β_u denotes the main direction of elevation angel and β_m denotes the variance of β_R^{Sca}. At last, the STCF can be written as

$$\rho_{h_{pq}h_{p'q'}}(t, \tau) = \sum_{l=1}^{L} c_l^2 \rho_{h_{l,pq}h_{l,p'q'}}(t, \tau). \quad (19)$$

Applying the Fourier transform to the STCF, the Doppler PSD can be obtained as

$$S_{h_{pq}h_{p'q'}}(f_D) = \sum_{l=1}^{L} c_l^2 \mathbf{F}\{\rho_{h_{l,pq}h_{l,p'q'}}(\tau)\} \quad (20)$$

where f_D is the Doppler frequency that $|f_D| < f_{\text{Rm}} + f_{\text{Tm}}$ and $\mathbf{F}\{\cdot\}$ indicates the Fourier transform. So Doppler PSD for each tap can be calculated as

$$S_{h_{l,pq}h_{l,p'q'}}(f_D) = \int_{-\infty}^{\infty} \rho_{h_{l,pq}h_{l,p'q'}}(\tau)e^{-j2\pi f_D \tau} d\tau. \quad (21)$$

The integral in (21) must be evaluated numerically in the case of the scattering components. As for the first tap and second tap, we can get the close-form expression.

$$S_{h_{1,pq}h_{1,p'q'}}(f_D) = e^{-jk_0(d(p,q)-d(p',q'))}\delta(f_D - H) \quad (22)$$

$$S_{h_{2,pq}h_{2,p'q'}}(f_D) = e^{-jk_0(d(p,R',q)-d(p',R',q'))}\delta(f - G) \quad (23)$$

where $\delta(\cdot)$ denotes the Dirac delta function, $G = f_{\text{Tm}}[\cos(\alpha_T^{\text{LoS}} - \gamma_T)\cos\beta_T^{\text{LoS}}\cos\xi_T + \sin\beta_T^{\text{LoS}}\sin\xi_T] + f_{\text{Rm}}[\cos(\alpha_R^{\text{LoS}} - \gamma_R)\cos\beta_R^{\text{LoS}}\cos]$, and $H = f_{Tm}[\cos(\alpha_T^{\text{Ref}} - \gamma_T)\cos\beta_T^{\text{Ref}}\cos\xi_T + \sin\beta_T^{\text{Ref}}\sin\xi_T] + f_{\text{Rm}}[\cos(\alpha_T^{\text{Ref}} - \gamma_R)\cos\beta_R^{\text{Ref}}]$.

TABLE I
DEFINITION OF SIGNIFICANT PARAMETERS.

Symbol	Definition
D	Distance between TX and RX
φ	Elevation angle between TX and RX
s_n	3D position of nth cluster
$\delta_R(\delta_T)$	Antenna element spacing at RX (TX)
$\alpha_R(\alpha_T)$	Azimuth angle of RX (TX) orientation
$\beta_R(\beta_T)$	Elevation angle of RX (TX) orientation
$h_1(h_2)$	Altitude of RX (TX)
$f_{\text{Rm}}(f_{\text{Tm}})$	Maximum Doppler frequency of RX (TX)
$\alpha_R^{\text{LoS}}(\beta_R^{\text{LoS}})$	AAoA/EAoA of LoS component
$\alpha_T^{\text{LoS}}(\beta_T^{\text{LoS}})$	AAoD/EAoD of LoS component
$\alpha_R^{\text{Ref}}(\beta_R^{\text{Ref}})$	AAoA/EAoA of reflection component
$\alpha_T^{\text{Ref}}(\beta_T^{\text{Ref}})$	AAoD/EAoD of reflection component
$d(A, B)$	Abbreviation of distance between A and B

IV. RESULTS AND ANALYSIS

In this section, some A2G channel statistic properties are presented based on the proposed wideband A2G GBSM. In the previous derivation, we use the reference model assuming infinite rays in each scatterers, and channel characteristics can be obtained by integral computation. However, integral computation is not easy to implement and time consuming. Therefore, a sum of sinusoids (SoS) simulation model based on proposed reference model is developed in this section by adopting finite number of rays. Method of equal volume (MEV) is applied to obtain discrete AoAs. The detailed description of this method is shown in [18]. Besides, some useful conclusions are given by analyzing the channel characteristics. In our simulation process, the following parameters are chosen unless otherwise specified: $f_c = 2\text{GHz}$, $D = 1000\text{m}$, $v_R = 10\text{m/s}$, $v_T = 30\text{m/s}$, $\gamma_T = \pi/4$, $\gamma_R = \pi/4$, $\xi_T = \pi/24$, $\alpha_T = \pi/12$, $\beta_T = \pi/6$, $\alpha_R = -\pi/3$, $\beta_R = -\pi/12$, $h_1 = 10\text{m}$, $\alpha_\mu = \pi$, $k = 10$, $\varphi = \pi/24$, $L = 5$.

Fig. 2 shows the temporal ACFs $\rho_{h_{pq}}(\tau)$ for reference model, simulation model, and simulation result calculated from simulation model using correlation function. Note that the path number of each tap is choosed as $N_l = 50$ in simulation model. It can be seen that temporal ACFs of three methods match with each other, which validates the correctness of the parameter generation method.
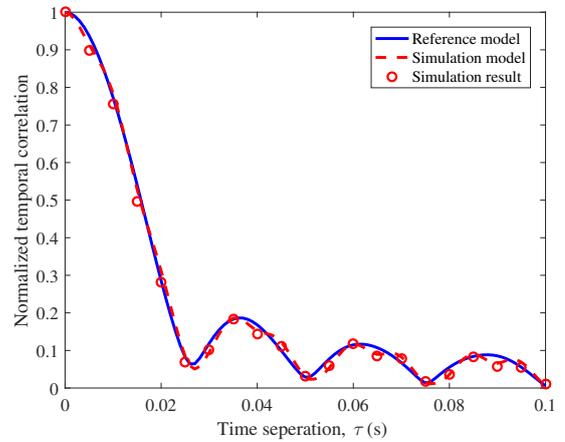

Fig. 2. Comparison of temporal ACFs with reference model, simulation model, and simulation result.

Fig. 3 shows the temporal ACFs for different UAV altitudes h_1. We can see that with the given scenario parameters, the higher communication altitude, the higher temporal correlation can be observed. It is because that the scattering space becomes smaller at higher altitude, which results in higher temporal correlation.

Fig. 4 presents the transmit spatial cross correlation functions (CCFs) for different antenna orientation azimuth angles. It can be observed that when the antenna point to the position
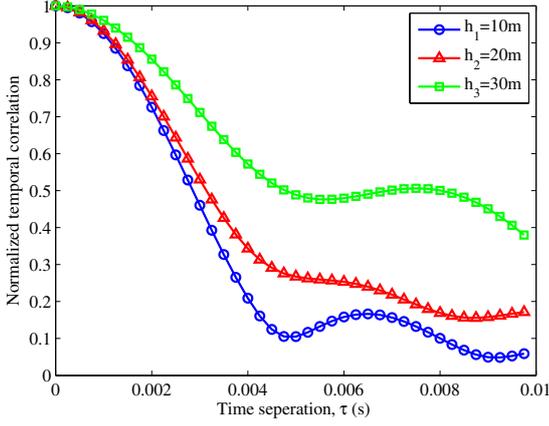
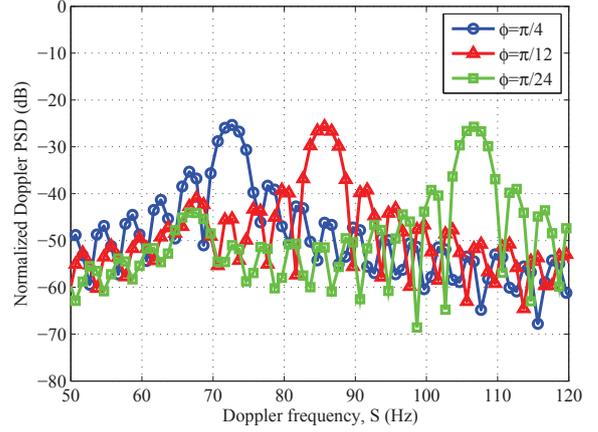Fig. 3. Temporal ACFs of different UAV altitudes.

Fig. 4. Spatial CCFs at TX side for different antenna orientation.

Fig. 5. Normalized Doppler PSDs of different communication elevation angels.
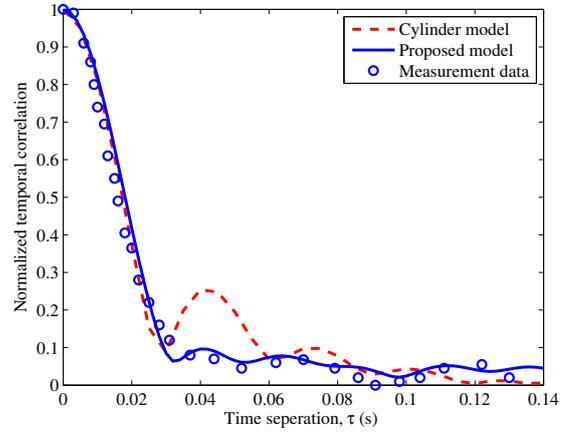

Fig. 6. Comparison of temporal ACFs for measurement data, proposed model, and cylinder model.

scatterers mainly distributed, the communication can realize more spatial diverse gain.

Fig. 5 illustrates the Doppler PSDs of scattering components with different A2G elevation angles. Since there is only one ray in both first tap and second tap, the Doppler PSDs become delta function in these two taps. We mainly concentrate on investigating Doppler PSDs of taps including scattering rays, i.e., the taps after the second tap. By analysis of Doppler PSD for scattering components in our simulation, it is observed that A2G communication elevation angles have great impacts on Doppler PSDs, as the results of A2G elevation angle change affects AoA and AoD of scattering components.

Fig. 6 presents the comparison of temporal ACF for measurement data [20], proposed simulation model, and single cylinder channel model proposed in [12]. With the parameters setting: $f_c = 2.5$GHz, $D = 1000$m, $v_R = 10$m/s, $v_T = 40$m/s, $\gamma_T = \pi$, $\gamma_R = \pi/4$, $\xi_T = 0$, $h_1 = 10$m, $\varphi = \pi/3$,the proposed model matches better with the measurement data in

temporal ACF that validate the practicality of our model.

V. CONCLUSIONS

In this paper, we have proposed a wideband MIMO A2G G-BSM, which has the ability to investigate the channel characteristics such as STCF and Doppler PSD at different time delays. Simulation results have shown that the A2G elevation angle and altitude of UAV have great impacts on channel characteristics. In the future, we plan to develop more accurate UAV channel models and investigate more UAV channel characteristics such as the non-stationary property of UAV channels [22].

REFERENCES

[1] T. Tomic, "Toward a fully autonomous UAV: research platform for indoor and outdoor urban search and rescue," *IEEE J. Robot. Automat.*, vol. 19, no. 3, pp. 46–56, Sept. 2012.

[2] S. Hayat, E. Yanmaz, and R. Muzaffar, "Survey on unmanned aerial vehicle networks for civil applications: a communications viewpoint," *IEEE Commun. Surveys Tuts.*, vol. 18, no. 4, pp. 2624-2661, Fourthquarter 2016.

[3] Y. Zeng, R. Zhang, and T. J. Lim, "Wireless communications with unmanned aerial vehicles: opportunities and challenges," *IEEE Commun. Mag.*, vol. 54, no. 5, pp. 36–42, May 2016.

[4] C.-X. Wang, J. Bian, J. Sun, W. Zhang, and M. Zhang, "A survey of 5G channel measurements and models," *IEEE Commun. Surveys Tuts.*, 2018, in press.

[5] A. Al-Hourani and K. Gomez, "Modeling cellular-to-UAV path-loss for suburban environments," *IEEE Commun. Lett.*, vol. 5, no. 99, pp. 1–5.

[6] D. W. Matolak and R. Sun, "Unmanned aircraft systems: air-ground channel characterization for future applications," *IEEE Trans. Veh. Technol.*, vol. 10, no. 2, pp. 79–85, Jun. 2015.

[7] E. Yanmaz, R. Kuschnig, and C. Bettstetter, "Channel measurements over 802.11a-based UAV-to-ground links," in *Proc. Globecom'11 Wi-UAV*, Dec. 2011, pp. 5–10.

[8] K. Takizawa, T. Kagawa, S. Lin, F. Ono, H. Tsuji, and R. Miura, "C-band aircraft-to-ground (A2G) radio channel measurement for unmanned aircraft systems," in *Proc. WPMC'14*, Sydney, NSW, Jun. 2014, pp. 754–758.

[9] Qixing Feng, J. McGeehan, E. K. Tameh, and A. R. Nix, "Path loss models for air-to-ground radio channels in urban environments," in *Proc. VTC'06*, Melbourne, Vic., Jun. 2006, pp. 2901–2905.

[10] Z. Shi, P. Xia, Z. Gao, L. Huang, and C. Chen, "Modeling of wireless channel between UAVs and vessel using the fdtd method," in *Proc. WiCOM'14*, Beijing, China, Sept. 2014, pp. 100–104.

[11] N. Goddemeier and C. Wietfeld, "Investigation of air-to-air channel characteristics and a UAV specific extension to the rice model," in *Proc. GLOBECOM'15*, San Diego, CA, USA, Dec. 2015, pp. 1-5.

[12] L. Zeng, X. Cheng, C. X. Wang, and X. Yin, "A 3D geometry-based stochastic channel model for UAV-MIMO channels," in *Proc. WCNC'17*, San Francisco, CA, USA, Sept. 2017, pp. 1–5.

[13] Y. Li and X. Cheng, "New deterministic and statistical simulation models for non-isotropic UAV-MIMO channels," in *Proc. WCSP'17*, Nanjing, China, Sept. 2017, pp. 1–6.

[14] L. Zeng, X. Cheng, C. X. Wang, and X. Yin, "Second order statistics of non-isotropic UAV Ricean fading channels," in *Proc. IEEE VTC'17-Fall*, Invited paper, Toronto, Canada, Sept. 2017, pp. 1-5.

[15] W. G. Newhall and J. H. Reed, "A geometric air-to-ground radio channel model," in *Proc. MILCOM'02*, Sept. 2002, pp. 632–636.

[16] M. Wentz and M. Stojanovic, "A MIMO radio channel model for low-altitude air-to-ground communication Systems," in *Proc. IEEE VTC'15*, Boston, MA, Sept. 2015, pp. 1–6.

[17] A. Shaw and K. Mohseni, "A fluid dynamic based coordination of a wireless sensor network of unmanned aerial vehicles: 3-D simulation and wireless communication characterization," *IEEE Sensors J.*, vol. 11, no. 3, pp. 722– 736, 2011.

[18] E. Yanmaz, R. Kuschnig, and C. Bettstetter, "Achieving AirGround Communications in 802.11 Networks with Three-Dimensional Aerial Mobility," in *Proc. IEEE INFOCOM'13*, Turin, Italy, Apr. 2013, pp. 120–124.

[19] Y. Yuan, C. X. Wang, X. Cheng, B. Ai, and D. I. Laurenson, "Novel 3D geometry-based stochastic models for non-isotropic MIMO vehicle-to-vhicle channels," *IEEE Trans. Wireless Commun.*, vol. 13, no. 1, pp. 298–309, Jan. 2014.

[20] M. Simunek, F. P. Fontan, and P. Pechac, "The uav low elevation propagation channel in urban areas: statistical analysis and time-series generator," *IEEE Trans. Antennas Propag.*, vol. 61, no. 7, pp. 3850–3858, Jul. 2013.

[21] H. Jiang, Z. Zhang, J. Dang, and L. Wu, "Analysis of semi-ellipsoid scattering channel models for vehicle-to-vehicle communication environments," in *Proc. IEEE VTC'17-Fall*, Sydney, NSW, 2017, pp. 1-6.

[22] S. Wu, C. X. Wang, e. H. M. Aggoune, M. M. Alwakeel, and X. H. You, "A general 3D non-stationary 5G wireless channel model," *IEEE Trans. Commun.*, vol. 66, no. 7, pp. 3065-3078, July 2018.